MULTIWAVELENGTH OBSERVATIONS OF THE SS 433 JETS

HERMAN L. MARSHALL[1], CLAUDE R. CANIZARES[1], TODD HILLWIG[2], AMY MIODUSZEWSKI[3],
MICHAEL RUPEN[3], NORBERT S. SCHULZ[1], MICHAEL NOWAK[1], AND SEBASTIAN HEINZ[4]

[1] Kavli Institute for Astrophysics and Space Research, Massachusetts Institute of Technology, 77 Massachusetts Avenue, Cambridge, MA 02139, USA;
hermanm@space.mit.edu, crc@space.mit.edu, nss@space.mit.edu, mnowak@space.mit.edu
[2] Department of Physics and Astronomy, Valparaiso University, Valparaiso, IN 46383, USA; todd.hillwig@valpo.edu
[3] NRAO, P.O. Box 2, Socorro, NM 87801, USA; amiodusz@nrao.edu, mrupen@aoc.nrao.edu
[4] Astronomy Department, 5408 Sterling Hall, University of Wisconsin, Madison, WI 53706, USA; heinzs@astro.wisc.edu
Received 2013 April 1; accepted 2013 July 30; published 2013 September 5

ABSTRACT

We present observations of the SS 433 jets using the *Chandra* High Energy Transmission Grating Spectrometer with contemporaneous optical and Very Long Baseline Array observations. The X-ray and optical emission line regions are found to be related but not coincident as the optical line emission persists for days while the X-ray emission lines fade in less than 5000 s. The line Doppler shifts from the optical and X-ray lines match well, indicating that they are less than 3×10^{14} cm apart. The jet Doppler shifts show aperiodic variations that could result from shocks in interactions with the local environment. These perturbations are consistent with a change in jet direction but not jet speed. The proper motions of the radio knots match the kinematic model only if the distance to SS 433 is 4.5 ± 0.2 kpc. Observations during eclipse show that the occulted emission is very hard, seen only above 2 keV and rising to comprise >50% of the flux at 8 keV. The soft X-ray emission lines from the jet are not blocked, constraining the jet length to $\gtrsim 2 \times 10^{12}$ cm. The base jet density is in the range 10^{10-13} cm^{-3}, in contrast to our previous estimate based on the Si XIII triplet, which is likely to have been affected by UV de-excitation. There is a clear overabundance of Ni by a factor of about 15 relative to the solar value, which may have resulted from an unusual supernova that formed the compact object.

Key words: stars: winds, outflows – X-rays: binaries – X-rays: individual (SS 433)

*Online-only material:* color figures

1. INTRODUCTION

SS 433 is still the only source that is known to have emission lines from ionized gas in a highly collimated jet from a compact object. Thus, it is an important member of the "microquasar" class of X-ray binaries (cf. Mirabel & Rodríguez 1999). For an early review of the source properties, see Margon (1984) or a more recent review by Fabrika (2004). The so-called kinematic model describes the Doppler shifts of the blueshifted and redshifted Hα lines as a pair of oppositely directed, precessing jets with speed, $v_j = 0.26c$ (Margon & Anderson 1989). The model has been used for over 30 yr when analyzing SS 433 data. There have been some updates to the parameters and to the model, most notably to add nutation with a period which is about half of the orbital period and to add small jet velocity variations at the orbital period (Blundell & Bowler 2005). Based on radio images, Blundell & Bowler (2005) also determined that the distance is 5.5 ± 0.2 kpc for a scale of 0.027 pc arcsec^{-1} but Stirling et al. (2002) argue that the distance should be somewhat smaller: 4.61 ± 0.35 kpc.

The precise description of the line positions was given by Margon & Anderson (1989): the jet orientation precesses with a 162.5 day period in a cone with half-angle 19°85 about an axis which is 78°83 to the line of sight. The lines from the jets are Doppler shifted with this period so that the maximum redshift is about 0.15 and the most extreme blueshift is about -0.08. We will use the reference phases and periods from Goranskij (1998), where the precession reference phase and precession period are JD 2,451,458.12 (updated by Gies et al. 2002) and 162.15 days; eclipses occur at the 13.08211 day binary period with reference phase of JD 2,450,023.62; and the jets nutate with period of 6.2877 days, ephemeris of JD 2,450,000.94, and

an amplitude $z_{\rm nut} = 0.009$ (Gies et al. 2002). For the remainder of this paper, we will use the truncated Julian date, defined by $\rm TJD \equiv JD - 2,450,000$. Assuming uniform outflow, the widths of the optical lines were used to estimate the opening angle of the jet: $\sim 5°$ (Begelman et al. 1980). For more details of the optical spectroscopy, see the reviews by Margon (1984) and Fabrika (2004).

SS 433 has radio jets oriented at a position angle of 100° (east of north) which show an oscillatory pattern that can be explained by helical motion of material flowing along ballistic trajectories (Hjellming & Johnston 1981). Using very long baseline interferometry observations of ejected knots, Vermeulen et al. (1993) confirmed the velocity of the jet and the kinematic model, although deviations of up to 10% were found from a sequence of observations spanning 40 days (Mioduszewski et al. 2003; Schillemat et al. 2004). The radio jets extend from the milliarcsecond scale to several arcseconds, a physical range of 10^{15-17} cm from the core. The optical emission lines originate in a region $\lesssim 3 \times 10^{15}$ cm across, based on light travel time arguments (Davidson & McCray 1980).

There is substantial literature on the X-ray emission from SS 433. Marshall et al. (1979) were the first to demonstrate that SS 433 is an X-ray source. Watson et al. (1986) showed that the X-ray lines were Doppler-shifted, locating at least some of the X-ray emission in the jets. Several groups used eclipse observations to estimate or limit the length of the X-ray-emitting portion of the jet, obtaining values of $\sim 10^{12}$ cm (Stewart et al. 1987; Kawai et al. 1989; Brinkmann et al. 1991; Antokhina et al. 1992). More recently, the jet lengths were modeled to obtain the binary mass ratio $q \equiv M_X/M_C \sim 0.3$, where M_X is the mass of the compact object and M_C is the mass of the companion star (Cherepashchuk et al. 2009). Brinkmann et al.
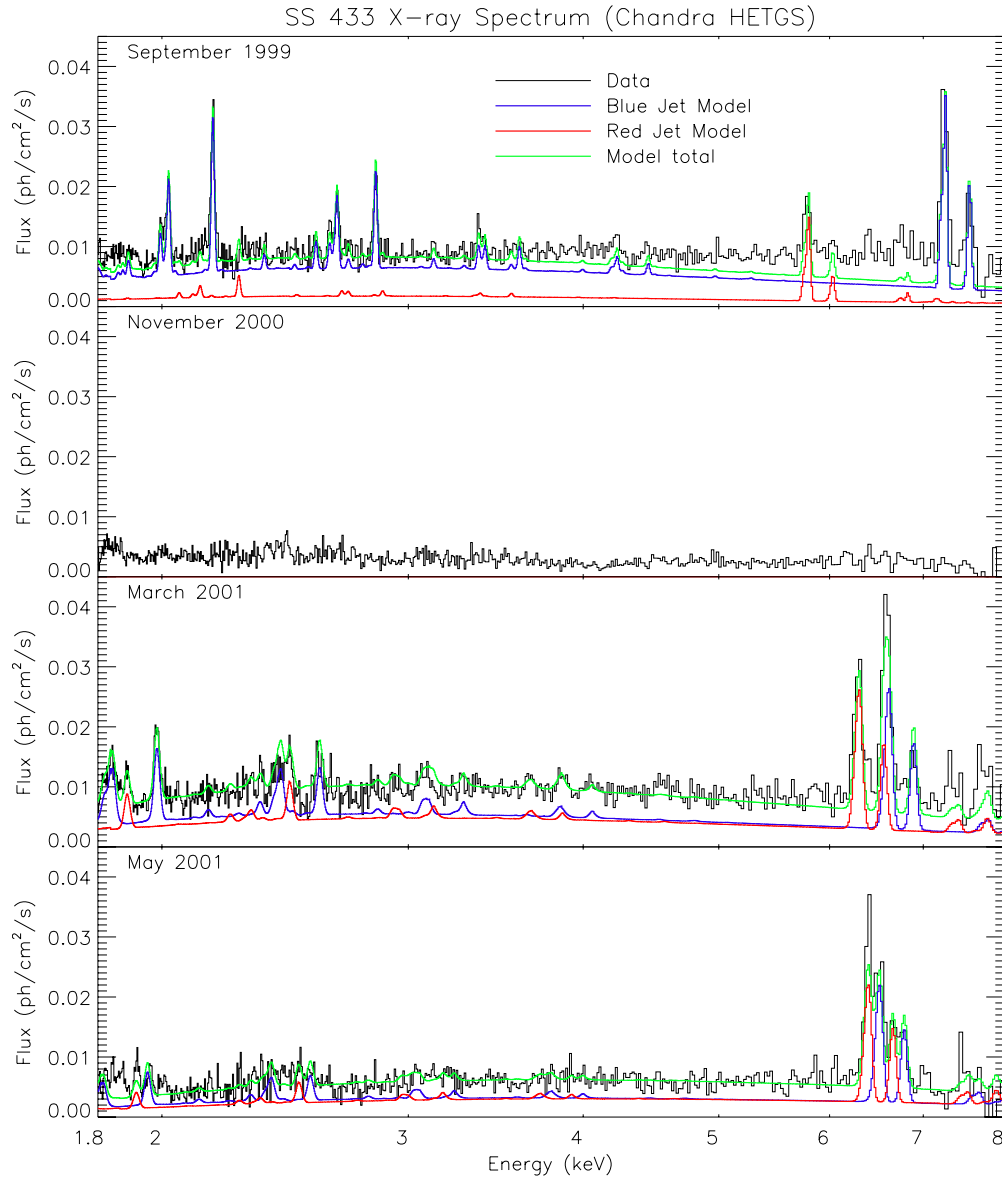
Figure 1. Four X-ray spectra of SS 433 taken with the *Chandra* High Energy Transmission Grating Spectrometer. The models were taken from Marshall et al. (2002) and Lopez et al. (2006) for the 1999 and 2001 March data sets. The model for the 2001 May data set was based on the model for 2001 March except that the Doppler shifts were changed to 0.0460 and 0.0265 (Namiki et al. 2003) and a factor of $0.85(E/1 \text{ keV})^{-0.5}$ was applied to reduce the continuum and the flux in the soft band. There are no clear emission lines in the 2000 November spectrum.

(A color version of this figure is available in the online journal.)

(1991) and Kotani et al. (1996) developed the model that the X-ray emission originates in thermal gas near the bases of the jets. The outflowing, cooling gas adiabatically expands and cools until kT drops to about 100 eV at which point the jet is thermally unstable (Brinkmann et al. 1988). Kotani et al. (1996) found that the redshifted Fe XXV line was fainter than the blueshifted line, after correcting for the expected Doppler diminution, leading them to conclude that the redward jet must be obscured by neutral material in an accretion disk.

Marshall et al. (2002, hereafter, Paper I) used an observation of SS 433 with the *Chandra* High Energy Transmission Grating Spectrometer (HETGS) to resolve the X-ray lines, detect fainter lines than previously observed, and measure lower energy lines that could not be readily detected in the *ASCA* observations. In Paper I, blueshifted lines dominated the spectrum and the redshifted lines were all relatively weak by comparison, so most work focused on modeling the blue jet (see Figure 1).

The jet Doppler shifts were determined very accurately due to the small scatter of the individual lines and the narrowness of their profiles, indicating that all line-emitting gas flows at the same speed. The jet bulk velocity was βc, where $\beta = 0.2699 \pm 0.0007$. This jet velocity was larger than the velocity inferred from optical emission lines by 2920 ± 440 km s^{-1}. Gaussian fits to the emission lines were all consistent with the same Doppler broadening: 1700 ± 80 km s^{-1} (FWHM). Relating this broadening to the maximum velocity due to beam divergence, the opening angle of the jet is $1°48 \pm 0°07$.[5]

Lopez et al. (2006) presented two more HETGS observations of SS 433; one showed no lines (2000 November) and the other was taken during eclipse (see Figure 1). In the eclipse observation (from 2001 March), lines from both the redshifted and

---

[5] Due to a coding error in Paper I, the opening angle was incorrectly reported to be $1°23 \pm 0°06$. We thank Dr. Rosario Iaria for pointing out this error.

Table 1
Chandra Spectroscopic Observations of SS 433

Date	Start TJD[a]	Observation ID	Exposure (ks)	MEG Rate (counts s^{-1})	ϕ_{prec}	ϕ_{orb}	Ref
1999 Sep 23	1445.04	106	28.7	1.59	0.92	0.67	Marshall et al. (2002)
2000 Nov 28	1877.07	1020	22.7	0.58	0.58	0.69	Lopez et al. (2006)
2001 Mar 16	1985.44	1019	23.6	1.58	0.25	0.97	Lopez et al. (2006)
2001 May 8	2038.09	1940	19.6	0.35	0.58	0.00	this work
2001 May 10	2039.95	1941	18.5	0.22	0.59	0.14	this work
2001 May 12	2041.96	1942	19.7	0.88	0.60	0.29	Namiki et al. (2003)
2005 Aug 6	3588.97	5512	21.0	2.31	0.14	0.54	this work
2005 Aug 12	3594.84	5513	48.2	1.75	0.18	0.01	this work
2005 Aug 15	3597.94	5514	73.1	2.08	0.20	0.25	this work
2005 Aug 17	3600.45	6360	59.1	2.07	0.21	0.44	this work

Note. [a] TJD is defined as JD − 2,450,000.

blueshifted jets were clearly detected and were of comparable strength. Previous X-ray observations of the SS 433 system during eclipse did not provide good detections of emission lines from the receding jet, leading to the suggestion that the entire inner region of the jets was eclipsed. However, the HETGS observation shows numerous emission lines from both jets.

Namiki et al. (2003) published the HETGS spectra from observation 2001 May 12 (see Table 1), the third of a set of three observations. Based on the width of the most highly ionized and blended Fe lines, they concluded that the base of jet subtends a larger angle than the remainder. Figure 1 illustrates that the combined *spectrum* from the data set shows highly blended lines and very weak low energy lines. The authors did not say why only the third observation was analyzed but it seems likely that it was because the source was somewhat fainter during observations 1940 and 1941 (see Table 1 and Figure 2).

Here, we present new observations of SS 433 using the HETGS as well as optical, hard X-ray, and Very Long Baseline Array (VLBA) observations obtained contemporaneously. The observations were designed to provide a high signal spectrum for testing the emission model, to obtain spectra during eclipse to test the obscuration of the red jet's emission, to accumulate sufficient observing time to detect nutational and precessional changes of the jets' Doppler shifts, and to obtain comparison data in other wavebands. Some preliminary results were reported earlier (Marshall 2006; Marshall et al. 2007), calling attention to a Doppler shift change over a 20 ks interval, much shorter than the nutational, orbital, or precession periods.

2. OBSERVATIONS AND DATA REDUCTION

2.1. Chandra X-Ray Observations

SS 433 was observed with the HETGS several times in 2005 August, as given in Table 1. Included in Table 1 are all the previous HETGS observations, with the count rate in the medium energy grating (MEG) band as well as the precession and orbital phases. The grating data and the count rates were extracted from the Transmission Grating Catalog (TGCat; Huenemoerder et al. 2011) as well as the light curves in 1000 s bins, shown in Figure 2 (for the first six observations) and Figure 3 for the 2005 observations. The count rate varies by almost a factor of 10 from year to year and by a factor of two to 4 on a time scale of days. The lowest count rate is not found during eclipse. During the 2005 observations, however, the total count rate varies by less than ±7% except during the eclipse, where the rate is about 15% low.

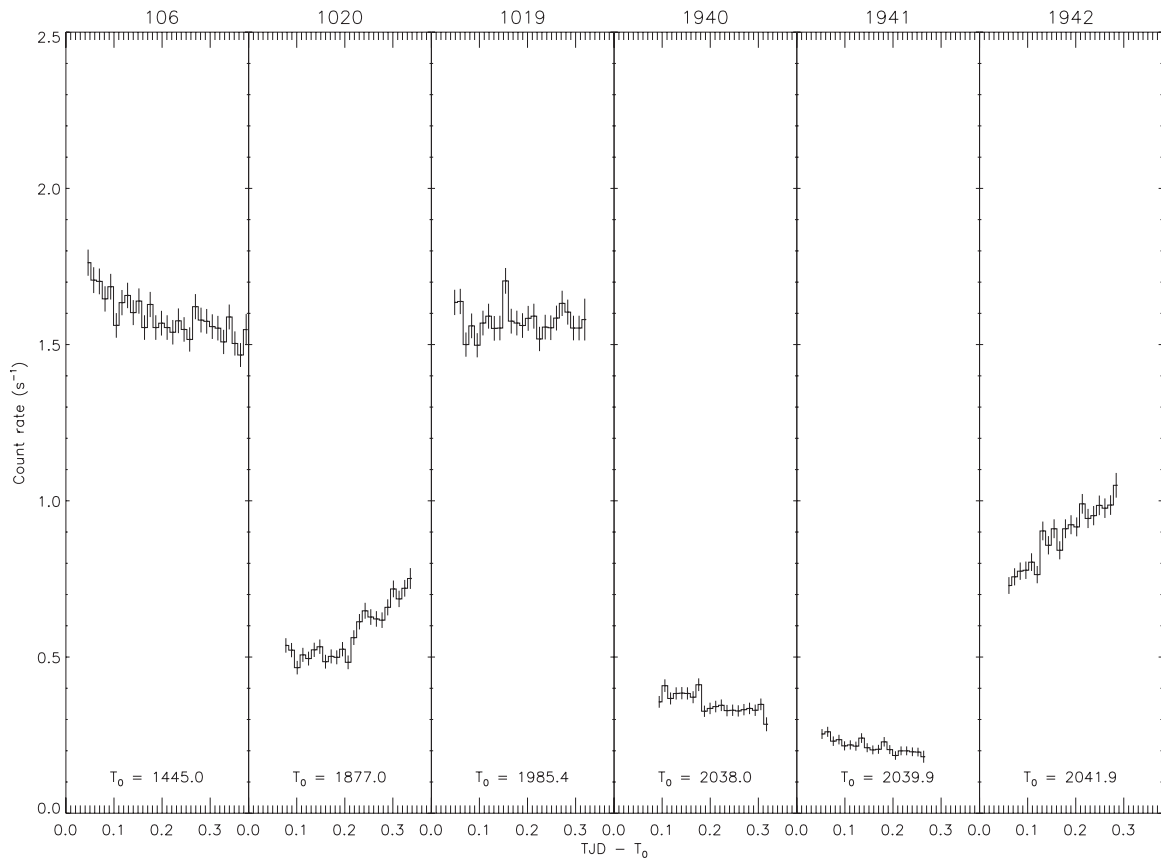**Table 2**
Rossi X-Ray Timing Explorer Observations of SS 433 in 2005

| Observation ID	Start Date (TJD)	Exposure (ks)
91092-01-01-00	3588.72	1.69
91092-01-02-00	3588.85	26.10
91092-02-01-02	3594.52	1.30
91092-02-01-04	3594.65	1.90
91092-02-01-00	3594.89	10.27
91092-02-01-01	3595.09	1.71
91092-02-07-01	3595.16	1.79
91092-02-01-03	3595.22	2.01
91092-02-02-00	3595.67	9.84
91092-02-03-00	3596.00	17.82
91092-02-04-00	3596.61	13.74
91092-02-05-00	3596.85	11.41
91092-02-06-01	3597.46	1.51
91092-02-06-02	3597.59	1.17
91092-02-06-00	3597.64	9.53
91092-02-07-00	3597.90	10.67
91092-02-08-00	3598.88	22.61

Due to the lack of lines in observation ID 1020, a short "trigger" observation was executed on 2005 August 6 (ObsID 5512). A quick look analysis showed significant emission lines, so the remaining observations were scheduled to start about a week later. Observation 5513 was taken during eclipse when the companion blocked part of the X-ray continuum. The predicted angle of the jet to the line of sight, α, varied from $69°$ to $77°$ during the 2005 observations. Within each observation, the data are essentially continuous. Light curves from all observations are included in Figure 3.

2.2. Rossi X-Ray Timing Explorer (RXTE) Observations

Rossi X-Ray Timing Explorer (*RXTE*) observations were obtained to overlap the 2005 *Chandra* HETGS observations. The observation time periods are given in Table 2. For each observation ID, the average count rates were determined from the standard data products in several bandpasses. These are shown in Figure 4. The count rates in each band are within 5% of being constant outside of eclipse, which is centered at TJD 3595.036 and spans about two days. Taking the eclipse to be from TJD 3594 to 3596.5, we can determine the average flux diminution relative to rates out of eclipse, from TJD 3596.5 to 3598.5. We find that the count rates dropped by $19.2\% \pm 0.4\%$, $35.9\% \pm 0.2\%$, $49.8\% \pm 0.5\%$, and $57\% \pm 3\%$

Figure 2. Light curves of SS 433 from the first six *Chandra* HETGS observations (see Table 1), using the MEG count rates (0.5–8 keV) in 1000 s bins from TGCat (Huenemoerder et al. 2011). The observation ID is given at the top of each panel. The X-ray source was in eclipse during observations 1019 and 1940, showing that the MEG count rates vary intrinsically by almost a factor of 10 and that the rates are not always lower during eclipses. A brightening factor of four occurred in less than 2 days between observations 1941 and 1942.
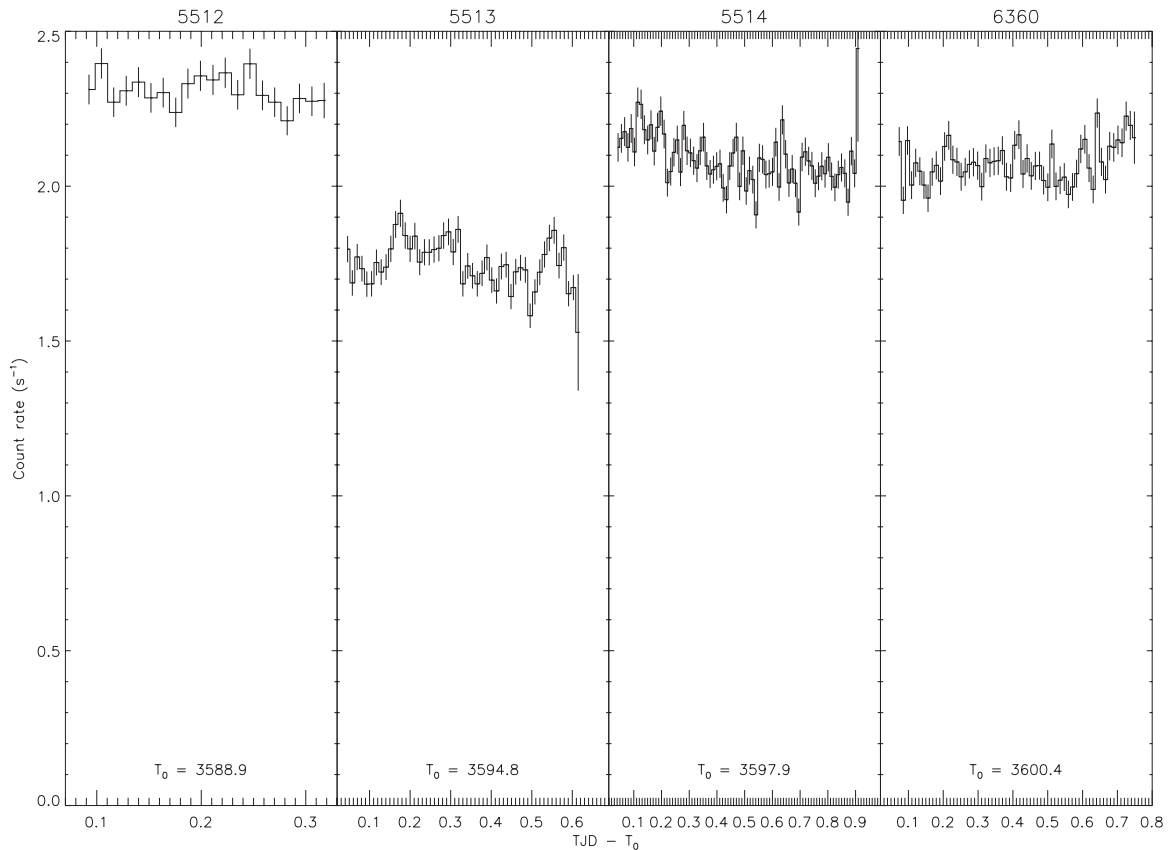
Figure 3. Same as Figure 2 but for the 2005 August *Chandra* observations. The source was in eclipse during observation 5513 but was otherwise constant within ±7%.

4
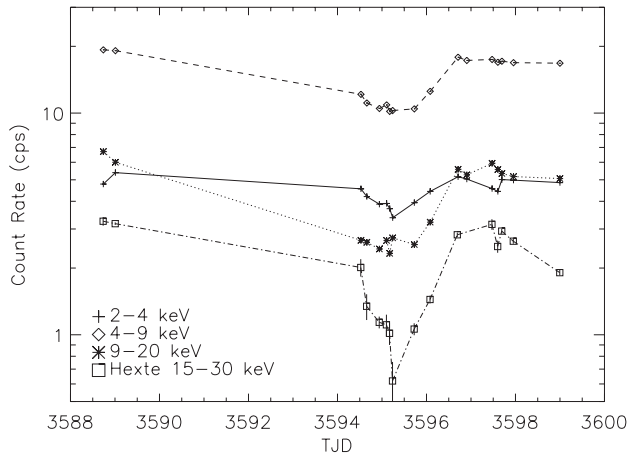
Figure 4. Count rates from *RXTE* observations taken in conjunction with the *Chandra* HETGS. Three broad Proportional Counter Array bands and one HEXTE band are plotted for each observation ID listed in Table 2. Error bars are purely statistical and do not reflect variations within data sets. Eclipse center is at TJD 3595.036, near the time when each band is low. Eclipse depth increases with energy, from 19% in the 2–4 keV band up to 57% in the 15–30 keV band (see text).

for the 2–4, 4–9, 9–20, and 15–30 keV bands, respectively. For the HEXTE 30–60 keV band, we obtained average count rates of 0.29 ± 0.04 counts s^{-1} in eclipse and 0.958 ± 0.044 outside of eclipse, for a 70% decrease during eclipse.
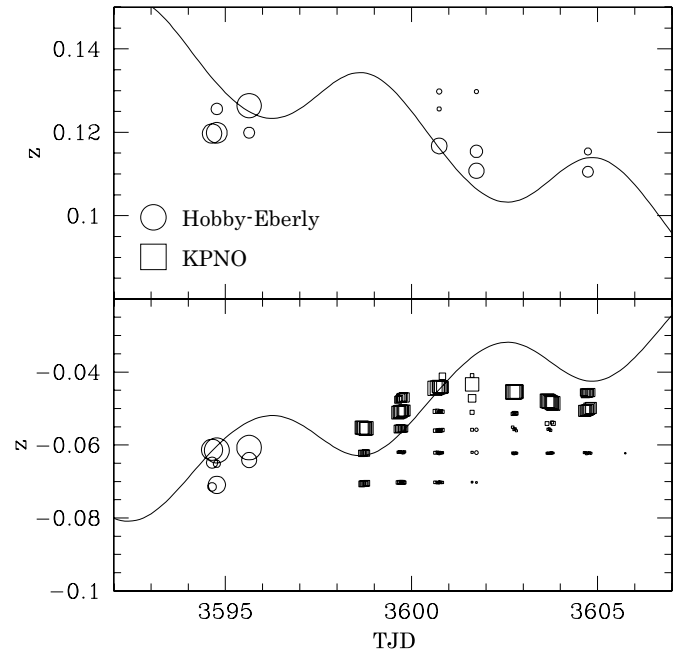
2.3. Optical Observations

Simultaneous optical spectra were obtained in order to model the relationship between the various emission regions. Data were obtained at the Hobby–Eberly Telescope (HET) with the Medium Resolution Spectrograph with $2''$ fibers (with spectral resolution $R \approx 5000$) and at the KPNO 2.1 m telescope using GoldCam with a $2''$ slit and grating 56 ($R \approx 4000$). The HET spectra were obtained generally only once per night while there were up to six KPNO spectra each night, at 40–50 minute intervals. Doppler shifts of the H-alpha lines are shown in Figure 5. A model of the Doppler shift variation is computed from the standard kinematic model but with a precessional time delay of 4 days, estimated to provide a better fit to the dominant lines. The effect of the time delay is to shift the precession model's expected Doppler shifts later in time. Precession phase jitter of 5–10 days—either later or earlier—has been found in many optical observations (Eikenberry et al. 2001).

As found by Vermeulen et al. (1993), emission lines appear at Doppler shifts that initially match the kinematic model (after accounting for phase jitter) but then persist for many days. Doppler shift deviations from the kinematic model can be of order 3000 km s^{-1}. Optical line FWHM values were 10–50 Å, giving Gaussian velocity dispersions of 200–1000 km s^{-1}. Emission line positions and equivalent widths were calculated using up to seven Gaussians with different centroids for lines that were clearly resolved. Line equivalent widths varied from 0.17 Å to 52 Å. Strongly blended lines were often fit using a single Gaussian. In these cases the line centers were not appreciably different than found by fitting several unresolved Gaussians. Likewise, most blended lines are dominated by a single component and thus the equivalent widths are also not greatly affected by a single fit.

2.4. VLBA Observations

VLBA observations at 15.4 GHz were obtained daily during part of the campaign from TJD 3591.7 to 3606.7, in 3 hr periods.

Figure 5. Doppler shifts from optical observations taken during the 2005 campaign as a function of TJD. Several spectra were obtained per night at KPNO. For most observations, the lines were fitted with several Gaussians at different Doppler shifts. The size of the symbol relates to the line strength. The lines provide a nominal ephemeris from the kinematic model of the jet Doppler shifts, with a time delay of 4 days.

The data were taken by alternating 2 minute observations of SS 433 with 1 minute on the phase calibrator J1912+0518. Because the phase calibrator was only $0°.42$ away from SS 433, absolute astrometry should be good to better than 0.2 mas. Calibrators J1800+7828 and J1907+0127 were also observed occasionally as check sources. The frequency range from 15.3495 GHz to 15.3810 GHz was covered in 8 MHz bandpasses. The data were reduced in the standard manner using NRAO's data reduction package, AIPS (Greisen 2003). Images were made with natural weighting, without the necessity of self-calibration.

Figure 6 shows eight images from the campaign. The beam is about 2 mas in the N–S direction and 1 mas in the E–W direction. The core position was stable to within astrometric accuracy at $(\alpha, \delta) = (19^h11^m49^s.56824, +04°58'57''.7632)$ (epoch J2000). The position angle of the jet is about $122°$ east of north, so the images were rotated $-32°$ to appear horizontal in the figure and referenced to the core. Two knots were tracked in the images; measurements are shown in Figure 7. The measured proper motions were 5.9 ± 0.6 mas day^{-1}, launched at TJD 3596.6 ± 0.1, and 7.14 ± 0.32 mas day^{-1}, launched at TJD 3597.72 ± 0.05. Given uncertainty in locating the core, we include a possible systematic error on the launch dates of ± 0.25 days.

2.5. X-Ray Doppler Shifts

From Figure 5, we expect that the Doppler shifts measured from the X-ray spectra will vary significantly over the several days covered by the *Chandra* observations. For this reason, the X-ray data were divided into 5 ks intervals to generate a series of spectra. Based on the results in Paper I, we expect that all the strong emission lines have the same Doppler shifts, so that the data for different lines were combined to improve the signal/noise. For specific, strong emission lines with rest energy E_0, the X-ray events from an energy range $[0.9 E_0, 1.17 E_0]$ were accumulated in 500 km s^{-1} bins to produce a velocity
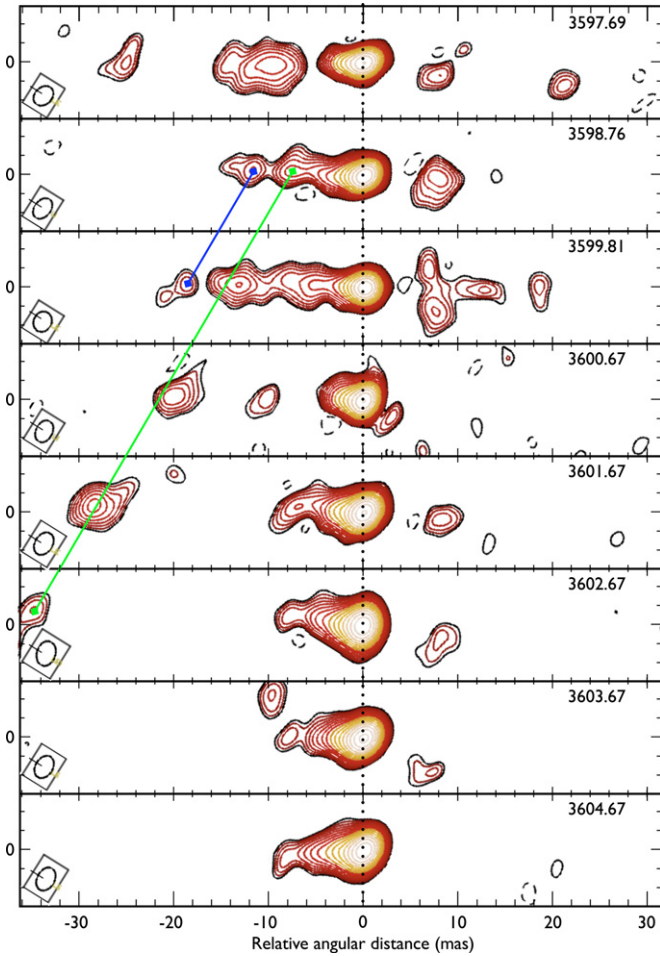
Figure 6. Images from the VLBA campaign rotated $-32°$ so that the jet is approximately horizontal. The beam is shown in the lower left corner of each image; the short line indicates E for each beam. Observation dates are given in TJD for each panel. Angular distances are marked in milliarcseconds relative to the map peak, whose astrometric position is consistent from image to image to within 0.2 mas. The lowest contour is 0.5 mJy beam^{-1}, with one negative contour at -0.5 mJy beam^{-1} (dashed), and contours increase by factors of $2^{1/2}$; maxima are between 60 and 100 mJy beam^{-1}. Green and blue lines connect components that were measured and shown in Figure 7.

(A color version of this figure is available in the online journal.)
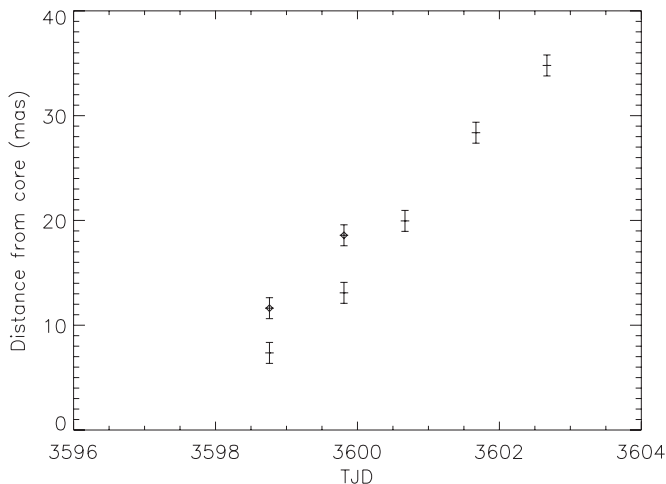
Figure 7. Distances (in milliarcseconds) from the core for two components in the VLBA images shown in Figure 6. Linear trends were fit to obtain the knots' proper motions and ejection dates. Horizontal lines span the observation periods, which were 3 hr for each observation.
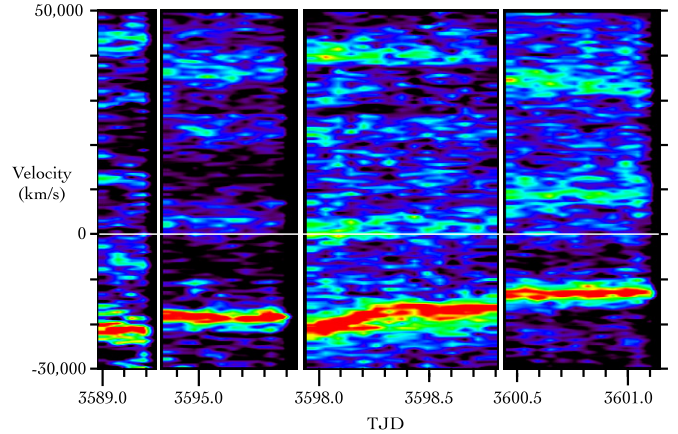
Figure 8. Trailed spectra from the *Chandra* observations. The lines of Mg XII, Si XIV, Fe XXVI, and Fe XXV were combined in 500 km s^{-1} velocity bins at 5 ks intervals and slightly smoothed for visualization. The red track follows the Doppler shift of the blueshifted emission lines near $-20,000$ km s^{-1}; the redshifted lines are barely visible between 30,000 km s^{-1} and 50,000 km s^{-1}. The weak features in the 0–10,000 km s^{-1} observed after TJD 3597 are due to weaker, adjacent lines in the spectra. Note that the blueshift scarcely varies during any given observation except near TJD 3598.0, where there is a clear linear increase of the blueshift by about 5000 km s^{-1} in a span of 0.3 days. The emission lines are not appreciably broadened temporally during the linear blueshift increase, indicating that most of the gas cools in less than 5000 s. The redshift barely changes during the observations but all Doppler shifts changed by about 3000 km s^{-1} between observations.

(A color version of this figure is available in the online journal.)
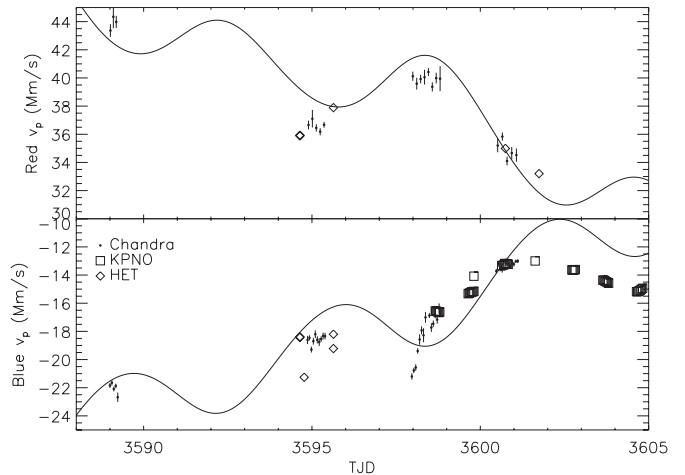
Figure 9. Doppler shifts from optical observations compared to the values obtained from *Chandra*. The Doppler shift model is the nominal ephemeris from the kinematic model, with a time delay of 4 days as plotted in Figure 5. Only the Doppler shifts for the strongest optical lines are shown, for clarity of comparison to the X-ray measurements. The optical and X-ray Doppler shifts generally agree within the uncertainties, when the results overlap.

profile every 5 ks. The Lyα lines of H-like Mg XII, Si XIV, and Fe XXVI were chosen, along with the Kα line from He-like Fe XXV. The result, in Figure 8, shows that (1) the blueshifted lines are substantially stronger than the redshifted lines, (2) the Doppler shifts mostly remain constant during 20–50 ks observations, (3) the Doppler shifts change by $\gtrsim 3000$ km s^{-1} during the day or more between observations, and, surprisingly, (4) a 5000 km s^{-1} shift was observed during a 0.3 day period starting at about TJD 3598.0.

Comparing the optical and X-ray Doppler shifts (Figure 9), we find that the Doppler shifts match to <1000 km s^{-1}. We can set an upper limit of 0.40 days for the maximum time

discrepancy between the optical and X-ray measurements of the blueshifted jet by noting that the X-ray measurements before TJD 3598.26 were all significantly more negative than the next optical measurement at TJD 3598.66. For the redshifted jet, the limit is obtained from the last optical measurement, at TJD 3601.75, which is significantly different from the last X-ray measurement, at TJD 3601.07, for an upper limit to the delay of 0.68 days.

As in Paper I, we assumed the system is composed of two perfectly opposed jets at an angle α to the line of sight. Then, the Doppler shifts of the blue and red jets are given by

$$z = \gamma(1 \pm \beta\mu) - 1, \tag{1}$$

where $v_j = \beta c$ is the velocity of the jet flow, $\gamma = (1 - \beta^2)^{-1/2}$, and $\mu = \cos\alpha$. As in the first paper, the line Doppler shifts were used to obtain an estimate of the γ by adding the redshifts to cancel the $\beta\mu$ terms and μ by subtracting redshifts:

$$\gamma = \frac{z_b + z_r}{2} + 1 \tag{2}$$

$$\mu = \frac{z_r - z_b}{2\gamma\beta}. \tag{3}$$

Shown in Figure 10 are the results from calculations using Equations (2) and (3), from which the jet velocity and angle to the line of sight can be determined under the assumption that the jets have the same speed and opposite directions. Given that only one of the two jets' Doppler shifts shows a significant trend near TJD 3598 while both of the derived parameters increase, it seems unlikely that both of these two assumptions are true, so we conclude that the jets' speeds or directions change independently on time scales of order 25 ks or less.

In order to determine which physical characteristics of the two jets differ on short time scales, we go back to the kinematic model and adjust its four parameters: the jet precession phase ϕ, precession angle θ, β, and the delay between a measurement of the X-ray Doppler shift and that measured in the optical band. The precession and nutation periods were fixed, along with the nutation phase and amplitude and parameters associated with the slight velocity variation with orbital period found by Blundell & Bowler (2005; observable in the panel showing β in Figure 10). The predicted variations are obtained by differentiating the equations for the Doppler shifts, holding all other parameters fixed. Coincidentally, the derivative of the jet blueshift with respect to either θ or β is very nearly zero at the end of the observation period (TJD 3602), so that the observed blueshift deviations are insensitive to modest changes of these two parameters.

In Figure 11, we show our best fit using small parameter adjustments. The position angle of the VLBA jet is very close to the expected value: 122° at TJD 3597.2. The expected VLBA proper motion, 8.6 mas day^{-1}, requires a change of β of -0.05 but changing other kinematic model parameters barely affects the predicted proper motion. While the blueshifts determined from the X-ray data are insensitive to $d\beta$ values as large as 0.05, the X-ray spectra's redshifts rule out values larger than 0.01.

Given that the knots appear to move ballistically, the low proper motions could be explained in this model if the jet decelerates by 20% between the location of the X-ray emission to where the VLBA knots appear about 1 day later, at about 5×10^{14} cm from the core. However, the optical emission
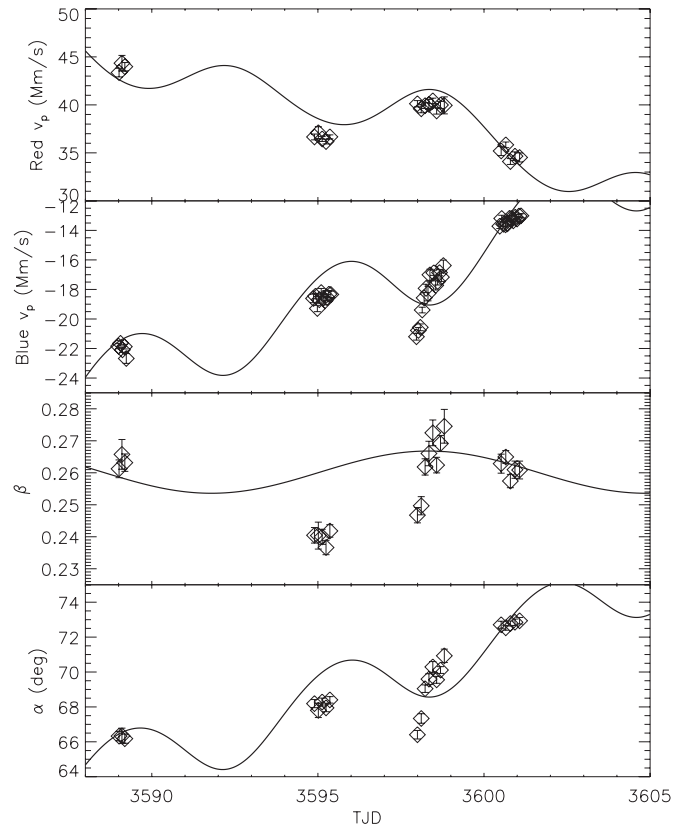

Figure 10. Doppler shifts for the redshifted and blueshifted X-ray emission lines and derived quantities. From the top, the panels show the Doppler shifts of the red jet (projected along the line of sight v_p), the projected Doppler velocities of the blue jet, the inferred jet speed relative to c, and the inferred angle to the line of sight (α). The smooth curves give the expected values for the nominal ephemeris for the kinematic model, with a precession delay of 4 days, as in Figure 9. The values of α and β are computed under the assumption that the blue and red jets are directly opposed with the same speed (see Equations (2) and (3)). The correlation of the computed jet parameters, α and β on TJD 3598 appear to result from a breakdown in these assumptions, rather than true velocity and jet angle correlations because the Doppler shift of the red jet does not vary on that day.

arises at about the same distance as the radio knots but the optical Doppler shifts agree well with those derived from the X-ray spectra, so this explanation seems unlikely. Alternatively, the distance to SS 433 could be 20% smaller than assumed: 4.5 ± 0.2 kpc, which is consistent with the value determined by Stirling et al. (2002).

The systematic deviations of the blueshifts by about -0.015 can only be accommodated in this approach by a precession phase shift of about -5 days (out of 162.5); it is as though the blueshifts are given by the model from 5 days prior (cf. Figure 10). The redshift deviations indicate a comparable phase shift but the systematic offset of about $+0.010$ could be explained by a combination of other parameter changes (e.g., by $d\beta = -0.02$ if $d\phi = 0$). Even with perturbations from the kinematic model, there are significant Doppler shift residuals up to 0.05 from the fit. The largest of these occurs near TJD 3598, reinforcing the conclusion that the kinematic model's assumptions do not hold on a time scale of 0.1 days.

3. X-RAY SPECTRA

The grating data were obtained from TGCat and reprocessed to reduce the spectral extraction widths because the default MEG region (100 pixels) overlaps the dispersed HEG
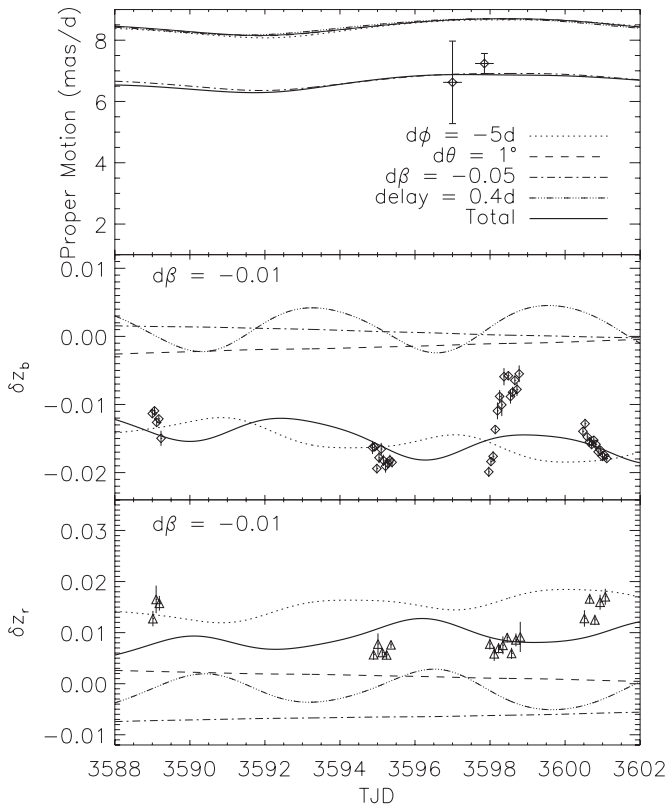
Figure 11. Comparison of the jet proper motion and the Doppler shift deviations from the nominal ephemeris to models with small adjustments of four parameters: precession phase ϕ, precession angle θ, β, and an X-ray to optical time delay (see text). Top: proper motion of the jet knots. Fitting the data requires that β decrease by 0.05; changes to other parameters have little effect. Middle: deviation of the blueshift from the nominal ephemeris. The systematic offset of about 0.015 is obtained only by a precession phase shift. Changing β or θ has little effect. Parameter adjustments are the same as in the top panel except for $d\beta$. Bottom: deviation of the redshift from the nominal ephemeris. Even after making adjustments to the kinematic model, significant Doppler shift residuals remain.

spectrum above 7 keV, so that the high energy events are not properly assigned to the HEG spectrum. After event assignment, the source extraction region was set to the standard width used by TGCat ($\pm 2''.39$). Background was selected from two regions from $2''.39$ to $7''.20$ from the dispersion. The MEG background spectrum was generally negligible for $1.6\,\text{Å} < \lambda < 18\,\text{Å}$ (0.69–7.75 keV), and is dominated by mirror scattering (consisting of $<2\%$ of the total flux), so is ignored for most analysis. Background is negligible for the entire HEG range of interest (1.25–16 Å or 0.77–10.0 keV) and is also dominated by mirror scattering at a similar level as in the MEG spectrum.

3.1. Eclipse

During eclipse, part of the X-ray emission is blocked, so we developed a spectrum of the occulted region by comparing to the non-eclipsed spectrum. Based on the *RXTE* light curves (Figure 4), we expect the eclipsed spectrum to be dominated by flux above 4 keV. We first combined the HETGS data taken outside of eclipse after correcting them for the changing blueshift using the data shown in Figure 8 where several strong lines are used to determine the mean blueshift in 5 ks intervals. See Section 2.5 for more details. These mean blueshifts were then fit to low order splines to obtain a smoothly varying function that could be applied to each X-ray event before binning into a spectrum. In order to avoid spurious features when comparing
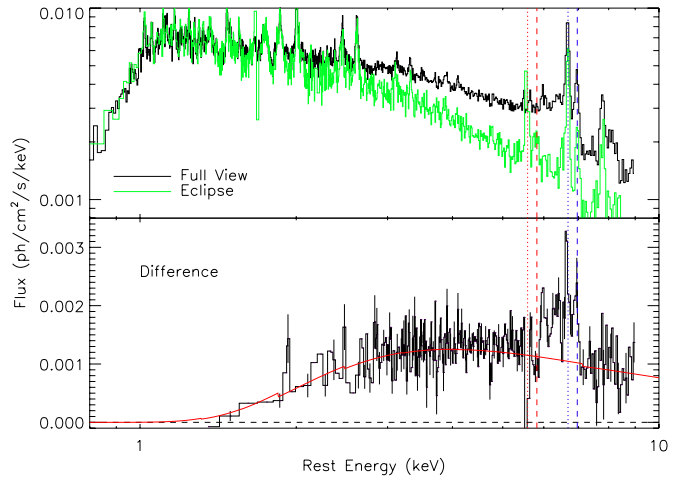
Figure 12. *Chandra* HETGS spectra of SS 433. Top panel: spectra outside of eclipse (black) and during eclipse (green). Bottom panel: difference between spectra in the top panel, giving a spectrum of the eclipsed emission region; the model (solid red line) is a simple continuum, described in the text. Note that the continuum below 2 keV and lines below 3 keV in the blueshifted jet spectrum are almost completely canceled in the subtraction. The two spectra in the top panel were corrected for the blueshifted jet's Doppler shift over several observations; the redshifted jet's lines of Fe XXV, S XVI, and Si XIV were excised from the full view spectra but a few weaker lines (e.g., Fe XXVI) from the redshifted jet in the non-eclipse spectra may show up in the difference spectrum. Vertical lines mark the redshifted (red) or blueshifted (blue) lines of Fe XXV (dotted) or Fe XXVI (dashed), as they are found in the eclipse spectrum; after excising the redshifted Fe XXV lines from the full view spectra before correcting for their blueshifts and combining, there is a corresponding negative residual in the difference spectrum. (A color version of this figure is available in the online journal.)

blueshifted jet spectra, four small wavelength ranges were excised from the data and response functions corresponding to unredshifted Fe I and the strongest redshifted lines: Fe XXV, S XVI, and Si XIV before combining in the reference spectrum.

The source did not vary significantly over the course of the campaign (Figure 3) and the spectra from non-eclipsed observations are nearly identical, so they are combined into one average non-eclipsed spectrum. Performing the same operation on the eclipsed data, we find that the resultant spectrum matches the non-eclipsed spectrum almost exactly below 2 keV (Figure 12). Importantly, the blue jet lines in the composite spectrum match those of the eclipse spectrum to better than 10%. Thus, it appears that the jets have not changed physically over the course of the campaign, spanning about 10 days, and that the blueshifted jet's cooler portions are fully visible during the eclipse.

As expected, the difference spectrum (Figure 12) is dominated by a hard continuum. Some of the features may be due to incomplete subtraction of weak red jet lines (e.g., Fe XXVI) or continuum. Also shown in Figure 12 is a cutoff power law continuum model of the occulted flux:

$$n_E = A(E/E_0)^{-\Gamma} e^{-N_H \sigma(E)} e^{-E/E_b}, \qquad (4)$$

where $A = 0.0016$ photons cm^{-2} s^{-1} keV^{-1}, $E_0 = 6$ keV is an arbitrary reference energy, $\Gamma = 0.4$ is the photon spectral index, $N_H = 3 \times 10^{22}$ cm^{-2} is the column density of cold gas along the line of sight, $\sigma(E)$ is the cross section to photoionize neutral gas with cosmic abundances, and $E_b = 20$ keV is the break energy. Most of the blue Fe XXV and Fe XXVI jet lines also appear to subtract out in this method of comparing the spectra. At most, 20% of the jet that provides the blue jet's Fe XXV line is blocked. Up to 30% of the blue jet's Fe XXVI could be blocked as well.

Table 3
Blue Jet Parameters from a Multi-temperature Model[a]

T (10^6 K)	EM (10^{57} cm^{-3})
12	0.66 ± 0.02
24	0.62 ± 0.05
48	<0.037
96	3.3 ± 0.2
192	<0.054
384	22.8 ± 0.3

Note. [a] Uncertainties and limits are for the 90% confidence level and six interesting parameters.

Thus, we confirm the result of Lopez et al. (2006) that these two lines of the blueshifted jet are mostly visible during eclipse. It is somewhat harder to determine how much of the red jet is blocked because it was somewhat fainter than the blue jet during this campaign, when there was a large difference in the blue and red Doppler shifts. However, models of the 2001 eclipse spectra indicate that the (somewhat blended) Fe XXV and Fe XXVI lines from both jets were similarly bright during the 2001 eclipse observations (Lopez et al. 2006; and Figure 1).

3.2. Modeling the Jet Emission Line Fluxes

As in Section 3.1, we combined all the X-ray spectra after correcting them for the changing blueshift in order to obtain a spectrum of the blueshifted jet. In this case, however, we also included the data from the eclipse observation with $E < 2.2$ keV, which is unaffected by the occultation, as found in Section 3.1. As in Paper I, the HEG and MEG spectra were modeled jointly using ISIS and the APED atomic data base of line emissivities and ionization balance. Starting from the model from Paper I, a moderately good fit was obtained to the line flux data with a four component model but based on a different temperature grid ($\times 2$ intervals in T), and at somewhat higher temperatures than found in Paper I. See Figure 13 for a comparison of the model with the HETGS data. Emission measures from the thermal model are given in Table 3. Other fit parameters were the turbulent velocity, $\sigma = 1800$ km s^{-1}, the metal overabundance factor, 6.2, the Ni overabundance factor, 89, and the interstellar absorption column density, $1.165 \pm 0.006 \times 10^{22}$ cm^{-2}.

We find no radiative recombination continuum features in these spectra and no other evidence for photoionization, in contrast with Paper I. The 9.10 Å line was misidentified as the Ne X radiative recombination continuum feature in Paper I, which we now identify with a Li-like Ni emission line. The misidentification resulted in part due to an early atomic data base with insufficient Ni lines. With these lines included and a solid detection of He-like Ni at 1.592 Å (rest frame), it is now clear that Ni lines are readily found because Ni is highly overabundant—by $\times 15$ relative to other metals.

The line width parameter from this fit appears to be too large for the long wavelength lines (see Figure 13). The HEG and MEG spectra were then jointly fit using Gaussian profiles at the positions of lines expected from the multi-temperature plasma modeling and observed in the data. The line widths were held fixed in five wavelength groups, while fitting for the line positions and normalizations. Results are given in Table 4. The continuum model was set to a simple power law for each group. Line strengths were found to be comparable to those of

Paper I, with the exceptions that the Fe XXVI and XXV lines are about twice as strong in the 2005 observation.

Line width measurements are given in Table 5. Systematic errors due to poor continuum modeling, unresolved blends modeled as single Gaussians, and unmodeled weak lines are estimated to be of order 100–150 km s^{-1}. Line blending, mostly important for $\lambda > 6.5$ Å, is also problematic for the Fe XXV line; this line dominates the average width in the 1.5–3.5 Å band, which is clearly larger than other values. The line widths are mostly somewhat larger than found in Paper I but comparable to the two values obtained by Namiki et al. (2003), who claimed that the ionized Fe lines were broader than the lines at 2 keV. Our examination of the observation they analyzed shows a noisy spectrum and at most very weak lines at 2 keV, to the point that they are not clearly detected (see Figure 1, where observation 1942 dominates the total flux). Given that Fe XXV consists of several unresolved lines and dominates the broad line measurement of Namiki et al. (2003) and that the lines may have blurred as the Doppler shift changed during the 20 ks observation, we are not confident that the Fe XXV lines are significantly broader than other lines in the spectrum. The smallest σ obtained here is consistent with the average obtained in Paper I, 729 ± 34 km s^{-1}, so we assume that this value is appropriate in modeling the jets for the remainder of the paper.

A close proxy to the spectrum of SS 433 was identified in the line-rich spectrum of θ^1 Ori C (Schulz et al. 2003), the brightest young O star in the Orion Nebula's Trapezium. A spectrum was derived from 12 observations in the TGCat archive (ObsIDs 3, 4, 2567, 2568, 7407-12, 8568, and 8569), totaling 398 ks of exposure, and then simply modified to provide a close match to the SS 433 continuum and overall line strengths by $f_{\mathrm{model}} = C_1 f_{\theta^1 \mathrm{OriC}} E^{0.5} + C_2$ and then applying the interstellar medium absorption correction, where E is energy in keV, and C_1 and C_2 were constants (6.5 and 0.0085 photons cm^{-2} s^{-1}, respectively). The modified spectrum was then Doppler broadened by a Gaussian with $\sigma = 1000$ km s^{-1}. The match to the SS 433 spectrum is generally good, as seen in Figure 14. There are notable exceptions: SS 433 shows the high temperature lines of Fe XXVI (1.78 Å) and Ni XXVII (1.60 Å). Ni is highly overabundant, as found in the APED fit and evidenced by the Ni XXVI and Ni XXV L lines in the 9.1–10.0 Å range (see Figure 13). Finally, the low temperature lines of Mg XI (9.2 Å) and Ne IX (13.5 Å) seen in θ^1 Ori C are not observed in SS 433. Thus, the spectrum of θ^1 Ori C is quite similar to that of SS 433 except that SS 433 has more high temperature gas, less gas at low temperatures, highly overabundant Ni relative to Fe, and more substantial Doppler broadening.

The comparison to θ^1 Ori C generally indicates that the X-ray emission is due to thermalized gas in both the O star and in the SS 433 jets. Schulz et al. (2003) and Gagné et al. (2005) provide a physical picture of the O star's spectrum using a magnetically channeled wind shock, based on papers by Babel & Montmerle (1997a, 1997b) and ud-Doula & Owocki (2002). This model provides high temperatures for the emission measure distribution and some Doppler broadening by turbulence is expected. We suggest that shocks provide the basic heating mechanism in SS 433 as well. It seems reasonable that a higher temperature component is required for SS 433 than is found in the O star wind, due to the mildly relativistic speeds of the jets. Of course, in SS 433, the heated gas is moving outward in opposed jets at $0.26c$ relative to the compact object in the system, so any shock-heating would take place in the frame of material already moving at high speed. The similarity of the SS
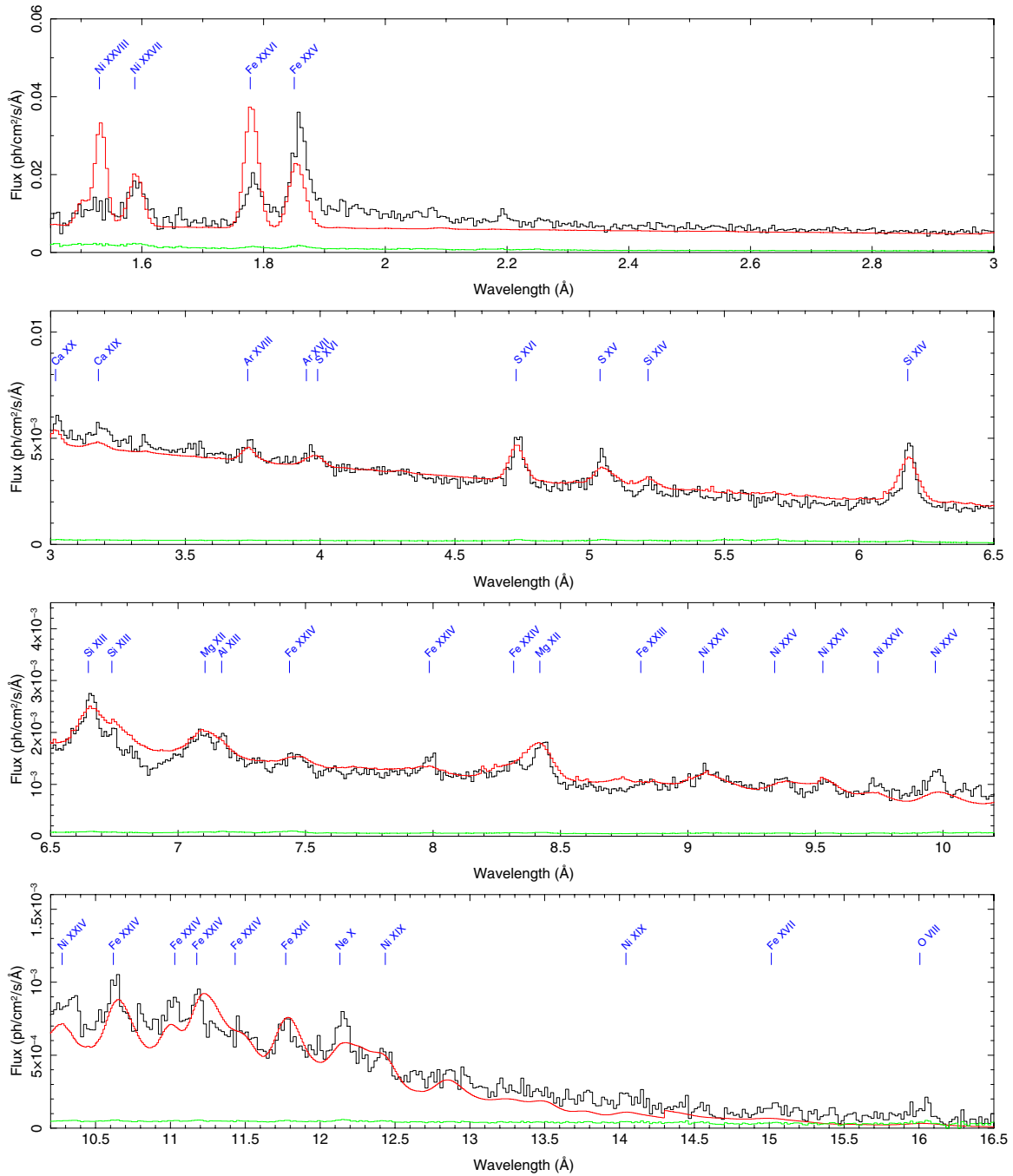
Figure 13. X-ray spectrum formed from the HEG data (top panel only) or combining the HEG and MEG data after correcting for the Doppler shift of the blueshifted jet. Green line: statistical uncertainties in the flux measurements. Red line: four temperature plasma model providing a generally adequate fit to the spectrum. Residuals near 2 Å are primarily due to the redshifted jet's continuum, which is somewhat weaker than those of the blueshifted jet. Line identifications are labeled where there are features in the spectrum and confirmed by the model.

(A color version of this figure is available in the online journal.)

433 spectrum to that of an O star does not provide an indication of the type of companion star, which is still a matter of some debate.

4. DISCUSSION AND SUMMARY

4.1. The Rapid Doppler Shift Change

The Doppler shifts of the blue jet lines are observed to undergo a rapid change during the 2005 observations with the *Chandra* HETGS. The change of $\sim$5000 km s^{-1} or $\Delta z = 0.017$ occurs on a time scale of 25 ks, much shorter than the time scale than any

of the known periodicities in the system due to precession, orbit, or nutation. Because the blueshifted jet's Doppler variations are insensitive to jet speed variations during the observation, we infer that the jet's direction was affected locally. Moreover, the emission lines are not appreciably broadened temporally—if the cooling time of the jet were much longer than 5 ks, then the variation observed in Figure 8 would be smeared horizontally, which is not observed. Thus, most of the gas must have cooled in less than 5000 s.

No large Doppler shift change was observed at the same time in the redshifted jet, indicating that the change is due to a local

Table 4
SS 433 Blueshifted Jet Lines[a]

λ_{rest} (Å)	λ_{obs} (Å)	Δz	Flux (10^{-6} photons cm^{-2} s^{-1})	Identification
1.532	1.526 ± 0.005	−0.0040 ± 0.0034	128. ± 30.	Ni XXVIII
1.592	1.592 ± 0.002	0.0003 ± 0.0011	279. ± 31.	Ni XXVII
1.780	1.786 ± 0.001	0.0032 ± 0.0007	272. ± 21.	Fe XXVI
1.855	1.860 ± 0.001	0.0030 ± 0.0003	713. ± 23.	Fe XXV
3.020	3.025 ± 0.005	0.0016 ± 0.0017	31. ± 6.	Ca XX
3.187	3.191 ± 0.004	0.0013 ± 0.0014	48. ± 6.	Ca XIX
3.733	3.740 ± 0.003	0.0020 ± 0.0008	31. ± 5.	Ar XVIII
3.962	3.970 ± 0.004	0.0021 ± 0.0011	29. ± 5.	Ar XVII, S XVI
4.729	4.735 ± 0.001	0.0013 ± 0.0003	111. ± 6.	S XVI
5.055	5.050 ± 0.002	−0.0011 ± 0.0004	89. ± 6.	S XV
5.217	5.224 ± 0.006	0.0013 ± 0.0012	20. ± 5.	Si XIV
6.182	6.186 ± 0.001	0.0006 ± 0.0001	170. ± 5.	Si XIV
6.648	6.652 ± 0.002	0.0005 ± 0.0002	82. ± 3.	Si XIIIr
6.740	6.735 ± 0.004	−0.0007 ± 0.0005	30. ± 3.	Si XIIIf
7.101	7.083 ± 0.003	−0.0024 ± 0.0004	43. ± 3.	Mg XII, Ni XXVI
7.173	7.172 ± 0.004	−0.0001 ± 0.0005	35. ± 3.	Al XIII
7.457	7.459 ± 0.006	0.0003 ± 0.0008	20. ± 3.	Fe XXIII/XXIV
7.989	7.984 ± 0.004	−0.0006 ± 0.0005	27. ± 2.	Fe XXIV
8.316	8.309 ± 0.004	−0.0009 ± 0.0004	33. ± 2.	Fe XXIV
8.421	8.425 ± 0.002	0.0005 ± 0.0002	66. ± 2.	Mg XII
8.815	8.851 ± 0.010	0.0041 ± 0.0011	12. ± 2.	Fe XXIII
9.075	9.080 ± 0.004	0.0005 ± 0.0004	22. ± 2.	Ni XXVI
9.372	9.371 ± 0.005	−0.0001 ± 0.0005	13. ± 2.	Ni XXVI/XXV
9.529	9.538 ± 0.006	0.0010 ± 0.0006	8. ± 2.	Ni XXIII
9.745	9.737 ± 0.007	−0.0008 ± 0.0007	6. ± 2.	Ni XXVI
9.970	9.973 ± 0.003	0.0003 ± 0.0003	26. ± 2.	Ni XXVI
10.634	10.633 ± 0.005	−0.0000 ± 0.0004	23. ± 2.	Fe XXIV
11.026	11.025 ± 0.007	−0.0001 ± 0.0006	18. ± 2.	Fe XXIV/XXIII
11.176	11.182 ± 0.004	0.0005 ± 0.0004	24. ± 3.	Fe XXIV
11.432	11.465 ± 0.017	0.0029 ± 0.0015	6. ± 2.	Fe XXIV
11.753	11.778 ± 0.008	0.0021 ± 0.0007	16. ± 3.	Fe XXIII/XXII
12.134	12.146 ± 0.006	0.0010 ± 0.0005	35. ± 4.	Ne X
12.435	12.426 ± 0.010	−0.0007 ± 0.0008	16. ± 3.	Ni XIX
14.060	14.109 ± 0.024	0.0035 ± 0.0017	9. ± 3.	Ni XIX
15.014	15.021 ± 0.029	0.0004 ± 0.0020	5. ± 2.	Fe VIII
16.006	16.022 ± 0.013	0.0010 ± 0.0008	14. ± 3.	O VIII

Note. [a] Rest wavelengths are computed for blends by applying weights equal to the fractional flux contribution to the blend, according to the multi-temperature plasma model.

**Table 5**
Blueshifted Jet Line Widths

Wavelength Range (Å)	v[a] (km s^{-1})
1.5–3.5	1900 ± 100
3.5–6.5	1100 ± 40
6.5–9.0	1260 ± 40
9.0–11.5	760 ± 40
11.5–16.0	950 ± 80

Note. [a] Velocity width (σ) of Gaussian line profiles. Uncertainties are statistical only; systematic errors of 100–150 km s^{-1} may be present due to line blends, continuum modeling, and unmodeled weak lines.

effect near the point where the heated plasma is accelerated to $0.26c$. One interpretation of these data is that the jets' terminal velocities are determined by environmental effects that perturb the direction of the jet. Velocity perturbations alone are insufficient to explain the large Doppler shift changes—either the −0.015 systematic offset from the kinematic model or the

0.05 residuals that remain after adjusting the parameters of the kinematic model. Angular deviations of order 3° along the direction of precession would be sufficient to explain the residuals of 0.05 in the blueshifted jet's Doppler shift.

From the concurrent VLBA monitoring, a jet knot was found that was ejected 0.22 ± 0.05 days before the start of observation 5514 and it appears that the blueshifted jet had already changed direction as the observation started. With a possible systematic uncertainty of about 0.25 days in the ejection time, it is possible that these two events are causally related. Radio-emitting knots were observed for several days, maintaining their discrete nature. By contrast, the X-ray-emitting region is continuously visible, smoothly shifting, and dominated by a single Doppler component. Thus, it seems that the SS 433 jets go through a transition from continuous flow to regularly spaced clumps—X-rays are emitted during the continuous flow, while the discrete knots produce most of the optical and radio emission. Such clumping could occur as a result of a thermal cooling instability (Brinkmann et al. 1988) or by slight variations in jet speed where slow moving flow is caught by faster moving material, perhaps causing shocks that reheat the gas and accelerating particles that produce radio emission via synchrotron radiation
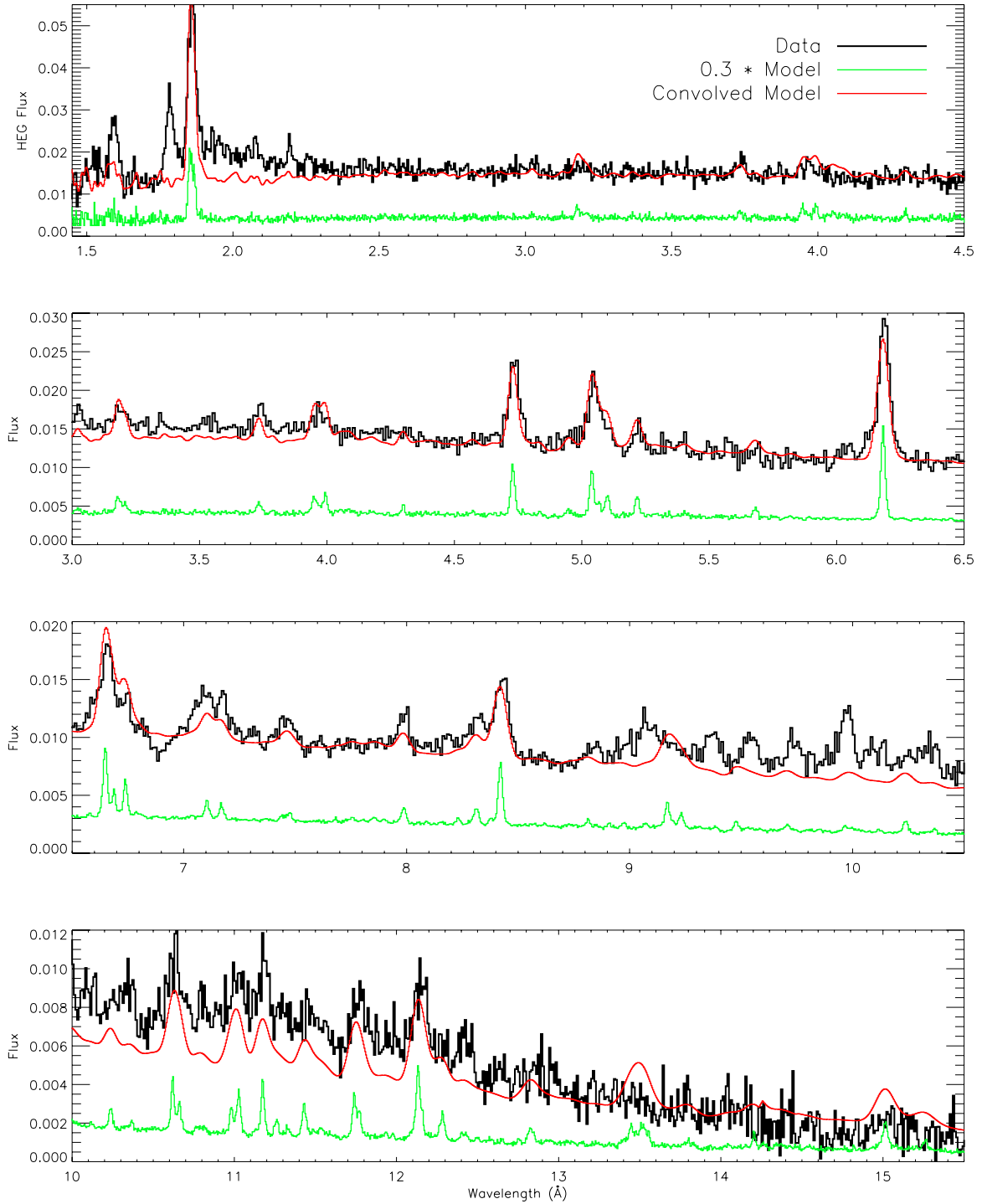
Figure 14. X-ray spectra of SS 433 after correcting for the Doppler shift of the blueshifted jet, compared to a model based on θ^1 Ori C. Green line: original spectrum of θ^1 Ori C, modified as described in the text and then scaled down by a factor of 0.3. Red line: spectrum of θ^1 Ori C, as modified and then Doppler broadened by a Gaussian with $\sigma = 1000$ km s^{-1}. The match to the SS 433 spectrum is generally good, with notable exceptions: SS 433 shows a much stronger Fe XXVI line at high temperature and Ni is highly overabundant (see Figure 13). Also the low temperature lines of Mg XI (9.2 Å) and Ne IX (13.5 Å) are not observed in SS 433.

(A color version of this figure is available in the online journal.)

(e.g., Migliari et al. 2005). Unfortunately, there was no HETGS coverage during the first knot ejection and the chances are fair that the 75 ks exposure of observation 5514 elapsed before the ejection of another radio knot.

4.2. Locating the Jet Origin

The location of the X-ray emission within the binary system can be constrained using various measurements from these observations. First off, limiting the cooling time to less than 5000 s requires that the X-ray-emitting gas moving at $0.26c$ be less than 4×10^{13} cm from the point at which the jet direction is set.

The similarity of the X-ray and optical Doppler shifts limits the time (and distance) between the X-ray emission and the optical emission to less than about 0.4 days (Section 2.5), or $<2.7 \times 10^{14}$ cm. Thus, it appears that there is no significant

deceleration of the jet between the optical and X-ray line emission regions. Combining with the distance limit from the jet base to the X-ray emission, the optical emission should occur $< 3.1 \times 10^{14}$ cm from the jet base. Note that Panferov (1999) obtained a similar estimate of the distance to the optical emission region: 4×10^{14} cm.

We limit the location of the hard X-ray emission using the eclipse observation. The source spectrum was remarkably steady during the 2005 campaign, so that it is straightforward to compare the spectrum during eclipse to other periods during the orbit. It is clear that the cool portions of the X-ray-emitting jet are not occulted during the eclipse. The difference spectrum (Figure 12) shows that the blocked emission is harder than the average, unblocked emission. The *RXTE* data (Section 2.2 and Levine et al. 2011) bolster this result: the eclipse depth increases with energy to the point that over half the flux above 15 keV is occulted during eclipse while less than 20% is blocked in the 2–4 keV band. Thus, the star is larger than previously estimated by Lopez et al. (2006) and large enough to block the highest temperature gas of both the redshifted and the blueshifted jets of the hardest emission during mid-eclipse. The eclipse is not detected when the jets are nearly perpendicular to the line of sight and the average X-ray count rates are similar to that in eclipse (Gies et al. 2002), suggesting self-obscuration by a flared disk at such precessional phases. The outer edge of the compact object's accretion disk could be optically thick to hard X-rays and very thick spatially, so that its angular size is comparable to the size of the companion star, as subtended from the compact object.[6] Levine et al. (2011) found mid-eclipse to be at TJD 2745.69 ± 0.18, which corresponds to an orbital phase of 0.080 ± 0.021—delayed with respect to the optical light minimum. The effect was first noticed by Kawai et al. (1989) and a similar result was found by Gies et al. (2002), who suggested that the companion has an extended cometary tail of optically thick gas trailing behind it in the orbital plane. Taken with the observation that the redshifted Fe XXV line has nearly identical flux as that of the blueshifted jet during eclipse and near the precessional "cross-over" point when the jets are nearly perpendicular to the line of sight (Lopez et al. 2006; and Figure 1), we conclude that this emission must occur farther than the donor star's Roche radius, $\sim 2 \times 10^{12}$ cm from the disk plane, for binary mass values reported by Hillwig & Gies (2008). This distance is comfortably smaller than that derived from the cooling time limit of 4×10^{13} cm.

We now place bounds on the electron density at the base of the jet. In order for the hottest line-producing component of the plasma to be in thermal equilibrium and visible during eclipse, the recombination time should be shorter and the radiative cooling time longer than the jet flow time to 10^{12} cm. Based on the abundances from the plasma fits, the cooling time for gas at 4×10^{8} K is $1000/n_{12}$ s, where n_{12} is the electron density in units of 10^{12} cm^{-3}. From the emission measure of this component, only when $n_{12} < 10$ is the cooling time long enough that the Fe XXVI is still visible during eclipse. For higher densities, the point at which the gas is heated to X-ray temperatures must be off of the disk in order to be visible during eclipse. The recombination time for Fe XXVI is $\sim 2/n_{12}$ s, so requiring that this time be short compared to the flow time gives $n_{12} > 0.01$.

Thus, the electron density should be in the range 10^{10-13} cm^{-3} to satisfy both requirements.

4.3. UV De-excitation of the Si XIII Triplet

In Paper I, we fit the profile of the Si XIII triplet in order to determine the resonance, intercombination, and forbidden line fluxes. The low value of the forbidden/intercombination line ratio was then used to estimate the density of the jet gas where Si XIII is prevalent, obtaining a value of $n_e \sim 10^{14}$ cm^{-3}. This value is substantially higher than estimated in the previous section. We now examine the possibility that this ratio is not a reliable density estimate for SS 433 because excitation by UV disk photons can suppress the forbidden line by depopulating the upper state before decay to the ground state. This mechanism has been invoked to explain the triplet line strengths of O stars (e.g., Kahn et al. 2001) and we follow a similar approach. Atomic data were taken from the online National Institute of Standards and Technology Atomic Spectra Database (Kramida et al. 2012).

The transition decay rate for the Si XIII forbidden line (from $2\,^{3}S$ to $1\,^{1}S$) is $A_f = 3.56 \times 10^{5}$ s^{-1} (Lin et al. 1977). UV excitation depends on the photon flux, F_ν, from the accretion disk at any of three transitions from $2\,^{3}S_1$ to $2\,^{3}P_J$, where J is 0, 1, or 2. The transitions have wavelengths $\lambda_J = (878.58, 865.14, 814.71)$ Å, upper level statistical weights $g_{2,J} = (1, 3, 5)$, and Einstein coefficients $A_{21,J} = (1.41, 1.391, 1.386) \times 10^{8}$ s^{-1} (Kelleher & Podobedova 2008). The excitation rate is

$$R_e = \int \frac{F_\nu}{h\nu} \sum_J \sigma_{\nu,J} d\nu \approx \sum_J \frac{\lambda_J F_\nu(\lambda_J)}{hc} \int \sigma_{\nu,J} d\nu$$

$$= \frac{1}{8\pi hc^2 g_1} \sum_J g_{2,J} A_{21,J} F_J \lambda_J^5, \qquad (5)$$

where $g_1 = 3$ is the statistical weight of the lower level, σ_ν is the transition's absorption cross section, and F_J is the flux density (in erg cm^{-2} s^{-1} Å^{-1}) of the disk at λ_J.

Gies et al. (2002) provided a range of disk temperatures for different values of the optical extinction of A_V, fitting blackbody spectra to FUV measurements from *Hubble Space Telescope*, UV values from Dolan et al. (1997), and optical data from Wagner (1986). They suggest that a model with $T = 21,000$ K and $A_V = 7.8$ is consistent with the observed UV and optical fluxes. However, they also say that a model with $T = 49,000$ K and $A_V = 8.2$ is marginally consistent with the data while a model with $T = 72,000$ K and $A_V = 8.4$ would be inconsistent with the data. For illustrative purposes, we assume a set of values: $A_V = (7.8, 7.8, 8.2, 8.4)$ for $T_4 \equiv T/(10^4$ K$) = (2.1, 4.5, 4.9, 7.2)$. Substituting the blackbody model into Equation (5), then

$$R_e = \frac{1}{4g_1} \sum_J \frac{g_J A_{21,J}}{e^{hc/(k\lambda_J T)} - 1} \qquad (6)$$

at the surface of the disk. For the four temperatures, we find $R_e/A_f = (0.1, 1.2, 11, 37)$, indicating that the UV flux is insufficient to depopulate the upper state of the forbidden line transition at the disk surface if its temperature is below 4.5×10^4 K but is large enough for higher disk temperatures—i.e., level depopulation by the FUV continuum is possible if $T/(10^4$ K$)$ is in the range 4.5–4.9, consistent with the FUV–optical spectra. As found in the last section, the jet's X-ray emission should be about 2×10^{12} cm from the disk surface; we find (projected)

---

6 Gies et al. (2002) suggested that a circumbinary disk is responsible for obscuring the central X-ray source when the accretion disk is viewed edge-on but in this case the X-ray flux should be *lower* than during eclipse, as a larger region is obscured.

disk radii in the range of 2–3×10^{12} cm, based on the dereddened optical fluxes (using dust correction by Fitzpatrick 1999; and $E(B - V) = A_V/3.1$), so dilution should not be significant. Given the uncertainty in the true disk temperature, we conclude that UV pumping may well be responsible for the low forbidden/intercombination line ratio found in Paper I, which led to an electron density estimate that was too high, $\sim 10^{14}$ cm^{-3} for gas with a temperature of order 10^7 K.

4.4. Ni Overabundance

The APED spectral fit and the comparison to the O star spectrum both indicate that Ni is highly overabundant. The APED fit (and our results from Paper I) indicate that all metals (particularly Fe) are overabundant by about a factor of six but the Ni abundance is $\times 15$ larger. We consider two possibilities for the source of Ni.

One possibility is that the excess Ni is inherent in the accreted gas, which is entrained in the jet via an interaction with the disk or companion's wind. This scenario requires that Ni is overabundant in the atmosphere of the companion. While Hillwig & Gies (2008) did not find Ni lines in the optical spectra they obtained of the companion star, no other elements appear to be particularly overabundant, including Fe. On the other hand, the companion spectra are diluted by emission from the disk and this dilution factor is not known a priori but determined by scaling the line strengths. The companion could be a post-asymptotic giant branch (AGB) A star like BD +48° 1220, which was found to have a super-solar abundance of Ni (Klochkova et al. 2007).

It also seems plausible that the excess Ni originated in the supernova (SN) that created the compact object. The SN would have deposited enriched material on the surface of the companion (perhaps as fall-back after the initial blast wave). However, in many SN models, most Ni would have been in the form of radioactive ^{56}Ni, which has a half-life of 6.1 days—much too short to be detected today, given that the system has been observed for at least 50 yr. For this model to apply, the SN would have to be of a rare type that produces as much stable Ni as Fe. Interestingly, Ni does seem to be $\gtrsim 10\times$ overabundant in the Crab Nebula (Dennefeld & Pequignot 1983; Henry 1984, 1986; Hudgins et al. 1990). Wanajo et al. (2009) developed such a SN model, starting with an 8.8 $M_\odot$ AGB star and invoking significant electron capture, that generates a Ni/Fe ratio that is 20 times the solar value due to the weak production of ^{56}Ni.

Another possibility is that Ni is formed in situ via an interaction of a jet with the disk wind. Such an interaction was proposed by Begelman et al. (2006) as a way to provide periodically redirected outflows from an inherently stably pointing jet. This scenario requires a high density of target material, which is feasible for a wind from a supercritically accreting disk. One problem with this model is that there is no particular reason to expect that only isotopes of Ni would result. We do not detect Mn and the Ar and Ca abundances appear to be similar to that of Fe.

5. SUMMARY

The 2005 campaign to observe SS 433 simultaneously at X-ray, optical, and radio wavelengths provided many ways to clarify its jet production mechanism.

1. A rapid change of one jet's Doppler shift was observed, changing by 5000 km s^{-1} in 25 ks, much faster than the precessional, orbital, or nutational time scales of the system. This rapid change may have coincided with the ejection of a radio-emitting knot, propagating ballistically away from the core.

2. The redshifted and blueshifted jets did not change at the same time, showing that the directions of the two jets are independently determined or affected by the environment.

3. Because the Doppler shift varied so quickly in one jet, the cooling time of the X-ray-emitting plasma was limited to <5000 s, limiting the distance from the jet launch site to the X-ray emission region to $<4 \times 10^{13}$ cm.

4. Observing discrete features in the radio band but not in the X-ray spectrum shows that the flow starts out continuous but then clumps to form knots.

5. Agreement between X-ray and optical Doppler shifts gives a consistent kinematic model, in conflict with the radio blob proper motions unless the distance to SS 433 is 4.5 ± 0.2 kpc.

6. The X-ray spectra were remarkably consistent before and after eclipse, providing an opportunity to determine the X-ray spectrum of the eclipsed emission, which is hard and mostly line-free. Observing emission lines during eclipse requires that the jet be longer than the Roche radius of the companion, $\sim 2 \times 10^{12}$ cm.

7. Modeling the jet's X-ray spectrum shows that Ni is $\times 15$ overabundant relative to other metals. We speculate that the SN that created the compact object in SS 433 was somewhat unusual, having generated as much stable Ni as Fe.

8. Disk UV flux could affect the Si XIII lines, possibly invalidating the use of their fluxes as a density diagnostic in this system.

9. Using various arguments relating to the jet plasma model, we derive a range for the electron density of 10^{10-13} cm^{-3} at the jet base.

10. We infer that shocks excite the X-ray-emitting gas to the observed temperatures, similar to situations found in young O stars.

REFERENCES

Antokhina, É. A., Seifina, E. V., & Cherepashchuk, A. M. 1992, AZh, 69, 282
Babel, J., & Montmerle, T. 1997a, ApJL, 485, L29
Babel, J., & Montmerle, T. 1997b, A&A, 323, 121
Begelman, M. C., Hatchett, S. P., McKee, C. F., Sarazin, C. L., & Arons, J. 1980, ApJ, 238, 722
Begelman, M. C., King, A. R., & Pringle, J. E. 2006, MNRAS, 370, 399
Blundell, K. M., & Bowler, M. G. 2005, ApJL, 622, L129
Brinkmann, W., Fink, H. H., Massaglia, S., Bodo, G., & Ferrari, A. 1988, A&A, 196, 313
Brinkmann, W., Kawai, N., Matsuoka, M., & Fink, H. H. 1991, A&A, 241, 112
Cherepashchuk, A. M., Sunyaev, R. A., Postnov, K. A., Antokhina, E. A., & Molkov, S. V. 2009, MNRAS, 397, 479

Davidson, K., & McCray, R. 1980, ApJ, 241, 1082
Dennefeld, M., & Pequignot, D. 1983, A&A, 127, 42
Dolan, J. F., Boyd, P. T., Fabrika, S., et al. 1997, A&A, 327, 648
Eikenberry, S. S., Cameron, P. B., Fierce, B. W., et al. 2001, ApJ, 561, 1027
Fabrika, S. 2004, ASPRv, 12, 1
Fitzpatrick, E. L. 1999, PASP, 111, 63
Gagné, M., Oksala, M. E., Cohen, D. H., et al. 2005, ApJ, 628, 986
Gies, D. R., McSwain, M. V., Riddle, R. L., et al. 2002, ApJ, 566, 1069
Goranskij, V. P. 1998, in 29th Conf. on Variable Star Research, ed. J. Dusek & M. Zejda (Brno: Brno Observatory and Planetarium), 103
Greisen, E. W. 2003, in Information Handling in Astronomy—Historical Vistas, ed. A. Heck (Astrophysics and Space Science Library, Vol. 285; Dordrecht: Kluwer), 109
Henry, R. B. C. 1984, ApJ, 281, 644
Henry, R. B. C. 1986, PASP, 98, 1044
Hillwig, T. C., & Gies, D. R. 2008, ApJL, 676, L37
Hjellming, R. M., & Johnston, K. J. 1981, ApJL, 246, L141
Hudgins, D., Herter, T., & Joyce, R. J. 1990, ApJL, 354, L57
Huenemoerder, D. P., Mitschang, A., Dewey, D., et al. 2011, AJ, 141, 129
Kahn, S. M., Leutenegger, M. A., Cottam, J., et al. 2001, A&A, 365, L312
Kawai, N., Matsuoka, M., Pan, H.-C., & Stewart, G. C. 1989, PASJ, 41, 491
Kelleher, D. E., & Podobedova, L. I. 2008, JPCRD, 37, 1285
Klochkova, V. G., Chentsov, E. L., Tavolzhanskaya, N. S., & Panchuk, V. E. 2007, ARep, 51, 642
Kotani, T., Kawai, N., Matsuoka, M., & Brinkmann, W. 1996, PASJ, 48, 619
Kramida, A., Ralchenko, Y., Reader, J., & NIST ASD Team. 2012, NIST Atomic Spectra Database, version 5.0, online at http://physics.nist.gov/asd
Levine, A. M., Bradt, H. V., Chakrabarty, D., Corbet, R. H. D., & Harris, R. J. 2011, ApJS, 196, 6
Lin, C. D., Johnson, W. R., & Dalgarno, A. 1977, PhRvA, 15, 154
Lopez, L. A., Marshall, H. L., Canizares, C. R., Schulz, N. S., & Kane, J. F. 2006, ApJ, 650, 338

Margon, B. 1984, ARA&A, 22, 507
Margon, B., & Anderson, S. F. 1989, ApJ, 347, 448
Marshall, F. E., Swank, J. H., Boldt, E. A., Holt, S. S., & Serlemitsos, P. J. 1979, ApJL, 230, L145
Marshall, H. 2006, in Proc. International Workshop on High Resolution X-ray Spectroscopy: Towards XEUS and Con-X, ed. G. Branduardi-Raymont, E20
Marshall, H. L., Canizares, C. R., Heinz, S., et al. 2007, in Relativistic Astrophysics Legacy and Cosmology—Einstein's Legacy, ed. B. Aschenbach, V. Burwitz, G. Hasinger, & B. Leibundgut (Berlin: Springer), 454
Marshall, H. L., Canizares, C. R., & Schulz, N. S. 2002, ApJ, 564, 941
Migliari, S., Fender, R. P., Blundell, K. M., Méndez, M., & van der Klis, M. 2005, MNRAS, 358, 860
Mioduszewski, A. J., Rupen, M. P., Walker, R. C., & Taylor, G. B. 2003, BAAS, 35, 1254
Mirabel, I. F., & Rodríguez, L. F. 1999, ARA&A, 37, 409
Namiki, M., Kawai, N., Kotani, T., & Makishima, K. 2003, PASJ, 55, 281
Panferov, A. A. 1999, A&A, 351, 156
Schillemat, K., Mioduszewski, A., Dhawan, V., & Rupen, M. 2004, BAAS, 36, 104.01
Schulz, N. S., Canizares, C., Huenemoerder, D., & Tibbets, K. 2003, ApJ, 595, 365
Stewart, G. C., Watson, M. G., Matsuoka, M., et al. 1987, MNRAS, 228, 293
Stirling, A. M., Jowett, F. H., Spencer, R. E., et al. 2002, MNRAS, 337, 657
ud-Doula, A., & Owocki, S. P. 2002, ApJ, 576, 413
Vermeulen, R. C., Murdin, P. G., van den Heuvel, E. P. J., et al. 1993, A&A, 270, 204
Wagner, R. M. 1986, ApJ, 308, 152
Wanajo, S., Nomoto, K., Janka, H.-T., Kitaura, F. S., & Müller, B. 2009, ApJ, 695, 208
Watson, M. G., Stewart, G. C., King, A. R., & Brinkmann, W. 1986, MNRAS, 222, 261